This article has been accepted for publication in IEEE Transactions on Antennas and Propagation. This is the author's version which has not been fully edited and content may change prior to final publication. Citation information: DOI 10.1109/TAP.2025.3573879

Electromagnetic Water Drop Model for Wet Antenna Attenuation Based on Near-Field Measurements

Jonas Tiede, *Graduate Student Member, IEEE*, Christian Chwala, Christian Herpers, Alexander H. Paulus, *Member, IEEE*, Uwe Siart, and Thomas F. Eibert, *Senior Member, IEEE*

***Abstract*—In order to better understand the wet antenna attenuation (WAA) effect in opportunistic rainfall estimation using commercial microwave links (CMLs), near-field measurements of a standard CML antenna under test (AUT) are performed under dry and wet conditions, and equivalent surface currents (ESCs) on the antenna radome are reconstructed. The far field of the wet AUT shows an overall reduced electric field magnitude around the boresight direction compared to the dry AUT. We deduce a simple and intuitive absorption-based electromagnetic drop model for corresponding local manipulations of the dry antenna ESC distribution at individual drops and show consistency of the modeled WAA with corresponding measurements. After validation, the model is applied to synthetic but realistic drop distributions as they accumulate during rain and dew. For both cases, justifiable WAA values are obtained, and a linear relation between WAA and the approximate radome area occupied by drops is demonstrated.**

***Index Terms*—antennas, commercial microwave links, near-field measurements, wet antenna attenuation.**

I. INTRODUCTION

UTILIZING commercial microwave links (CMLs) for quantitative rainfall estimation (QPE) [1], [2] has shown to provide country-wide rainfall measurements with quality almost on-par with weather radar data [3], [4]. CML data makes it even possible to generate rainfall maps with high spatial and temporal resolution in data-scarce areas, i.e., with low availability of otherwise common weather monitoring instrumentation [5]. The capability of using existing infrastructure without the expenses of additional hardware and potentially associated construction or assembly efforts qualify CML-QPE as a powerful tool to be used in flood forecasting [6], [7].

A. Motivation

Alongside the aforementioned advantages, processing the raw CML data poses several challenges. One of the common difficulties is to estimate the share of path loss which is contributed by water droplets settling on the antenna radome, e.g., during a precipitation event or due to a large relative humidity. These water residuals on the antenna radome interact with the radiation fields and, associated to this, in general lead to a disturbed far-field (FF) performance of the antenna. Commonly, this contribution to path loss is denoted as wet antenna attenuation (WAA) since the overall path loss is increased compared to conditions with a dry antenna. The consequence of WAA is usually an overestimation of the rain rate derived from CML data during a rainfall event. Moreover, even after a precipitation event has passed, the antenna radome can remain in a wet condition and slowly dry off, leading to prolonged periods of additional path loss without actual rainfall present. This also applies to dew droplets accumulating over the area of the antenna radome, causing attenuation even during the complete absence of rainfall [8], [9]. Overall, the undesirable WAA effect requires a correction in CML path loss time series in order to increase the accuracy of CML-QPE.

The problem of water presence on large microwave antenna radomes has been addressed by analytical methods, where, e.g., [10] suggests to consider just the attenuation of a plane wave passing through a continuous and infinite-plane water slab in free space. For common directional CML antennas with a large radome diameter in terms of wavelength, such approaches can be useful to obtain a rough estimate of the impact of radome wetness on the transmission performance. A corresponding WAA correction technique, using an infinite-plane multi-layer medium which accounts also for the radome, has been described in [11], suggesting to apply the method to recorded CML time series.

Numerical simulations of a wet radome alone, i.e., without a surrounding antenna structure, and approximating it as flat and infinitely large by utilizing a unit cell model, were performed for S-band frequencies in [12]. Based on Maxwell-Garnett's theory, the raindrop distribution together with the intermediate air was substituted by a layer of a homogeneous effective medium. For lower frequencies in the S-band, this approximation justifiably neglects physical effects at the individual water drops. With increasing frequency, the corresponding error, however, will enlarge. Especially for frequencies extending into and beyond the Ka-band (which is typical for CMLs), a more realistic model considering individual water drops on an infinitely large radome was introduced in [13]. Parameters including radome thickness, shape, and material properties most likely also play important roles, but they are

---

Submitted on... This work was supported by the Deutsche Forschungsgemeinschaft (DFG, German Research Foundation) under project ID 432287169.

J. Tiede, C. Herpers, A. H. Paulus, U. Siart, and T. F. Eibert are with the Department of Electrical Engineering, School of Computation, Information and Technology, Technical University of Munich, 80290 Munich, Germany (e-mail: jonas.tiede@tum.de).

C. Chwala is with the Karlsruhe Institute of Technology, Institute of Meteorology and Climate Research (IMK-IFU), Garmisch-Partenkirchen, and the University of Augsburg, Institute of Geography, 86159 Augsburg, Germany.

C. Herpers is now also with the Fraunhofer EMFT Institute for Electronic Microsystems and Solid State Technologies, 80686 Munich, Germany.

not precisely known in general because this information is typically not made available by the antenna manufacturers. Nevertheless, the general impact of radome wetness on the radiation capabilities of an associated CML antenna has been reproduced qualitatively with the model in [13] also in terms of the reflection of a certain portion of the incident power by the drop layer. Simulations and measurements with water films of controllable thickness have been performed on a small exemplary horn antenna [14], where the reflectivity of the antenna was also observed to depend on the water film thickness.

Other approaches model the WAA as being constant during rainfall events [15], as a process exponentially converging to a set maximum value over time [16], or as a quantity which is dependent on the rain rate [11], [17], [18]. The reported values of WAA are in the range of two to three decibels, but in some datasets, much higher values of up to 9 dB were also observed during extremely heavy rainfall events with rather short CMLs [19].

Recently, measured path attenuation and simultaneously recorded rainfall data was converted into a residual WAA time series in a Czech E-band CML dataset [20]. Using the WAA time series, a long short-term memory neural network was trained with the data in order to predict the WAA. With the rapidly emerging capabilities in utilizing artificial intelligence for large amounts of data, such approaches might be promising especially for large CML datasets as they could be obtained by merging individual datasets into larger ones [21]. However, reliable reference data along a CML path is required to derive such a residual WAA time series.

Altogether, heuristic WAA estimation methods using CML time series are currently complemented by simulation and experimental work which has been done to investigate idealized or isolated effects related to antenna wetness. However, a sufficiently accurate but yet simple enough electromagnetic drop model for the WAA which is close to the underlying physical processes is currently not available. Such an approach would allow deducing the WAA from, e.g., information about the water drop distribution on the antenna radome. However, dedicated quantitative observations of the WAA effect are generally only feasible in certain experimental setups or in rare cases where very reliable reference data for the path-averaged rain rate is available. Furthermore, accurate observations of the wetness conditions on an antenna radome are usually also rare. Without sufficient understanding of the physics of WAA, it is, thus, difficult to extrapolate these few findings from experimental observations directly towards universal WAA correction methods that can be applied to arbitrary CML datasets for rainfall estimation.

B. Our Contribution

In this work, we perform NF measurements of a highly directive, off-the-shelf Ka-band CML antenna under dry and wet conditions, as well as with controlled temperature in order to avoid temperature dependencies. Based on these measurements and inspired by the concept of physical optics (PO) [22], [23], we derive a simple modelling technique for the interaction effects of individual water drops with the incident electromagnetic field from the antenna under test (AUT) with regard to the WAA. The drop model replicates underlying measurements with high accuracy. On this foundation, a linear relation between the WAA (in dB) and the total radome surface area covered by water drops is derived. With this linear function, the WAA can be readily estimated for this particular AUT and frequency from only rough information about the amount of wetness on the radome.

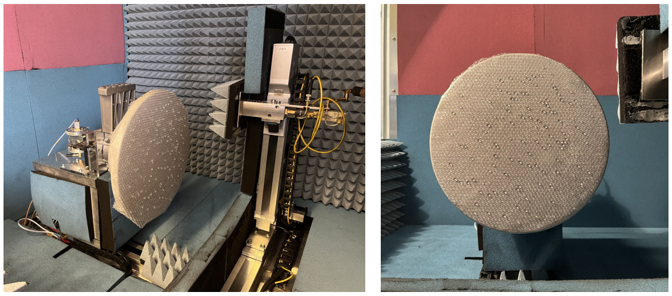
(a) (b)

Fig. 1. Bubble foil attached to the AUT inside the anechoic chamber. Some of the bubbles are filled with distilled water. (a) Perspective view, (b) front view.

Originating from these observations, new possibilities towards WAA correction emerge. Further development of the proposed drop modelling technique will allow to extrapolate corresponding observations to further frequencies, antennas and water formations on antenna radomes. This would then make WAA predictions possible even for yet unseen configurations and lay a foundation for very flexible new WAA correction methods. Altogether, the analysis at hand constitutes a considerable step towards the development of new physics-based WAA estimation models.

C. Outline

In Section II, the measurement setup, the procedure to obtain the ESCs and the preprocessing methods are described. Based on the results, the drop model is introduced and evaluated in Section III. The implications are generalized by investigating synthetic drop distributions in Section IV before summarizing and concluding the findings in Section V, together with an evaluation on how the presented electromagnetic drop model could inspire future methods for time-series based CML-QPE.

II. EQUIVALENT SURFACE CURRENTS FROM DRY AND WET ANTENNA NF MEASUREMENTS

A. Surface Equivalence Principle

Figure 1 shows the (wet) AUT, manufactured by Ericsson under the product name ANT2 0.3 38 HPX, mounted in the used anechoic chamber [24], [25]. The operating frequency is 38.5 GHz and the diameter of the plastic radome is $R = 38.2\,\text{cm}$, corresponding to an electrical diameter of about $49\,\lambda_0$ with the free-space wavelength λ_0. Denoting the surface enclosing the AUT by S, the electric field $\boldsymbol{E}(\boldsymbol{r})$ which

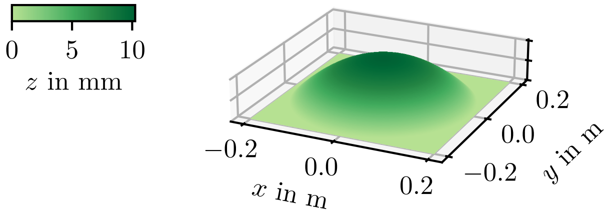

Fig. 2. The surface $\tilde{S}$, which coincides with the paraboloidal radome.

is produced by the antenna in the exterior of S can be written as

$$\boldsymbol{E}(\boldsymbol{r}) = \oiint_S \left[\bar{\boldsymbol{G}}_J^E\left(\boldsymbol{r},\boldsymbol{r}'\right)\cdot\boldsymbol{J}_S\left(\boldsymbol{r}'\right) + \bar{\boldsymbol{G}}_M^E\left(\boldsymbol{r},\boldsymbol{r}'\right)\cdot\boldsymbol{M}_S\left(\boldsymbol{r}'\right)\right]\mathrm{d}a' \tag{1}$$

on the basis of the well-known surface equivalence principle [26] (SEP), where $\bar{\boldsymbol{G}}_J^E$ and $\bar{\boldsymbol{G}}_M^E$ are dyadic Green's functions for the electric field produced by the tangential electric and magnetic surface currents $\boldsymbol{J}_S$ and $\boldsymbol{M}_S$ which are defined on S. Figure 2 shows the bulging front square $\tilde{S} \subsetneq S$, constituted by a circular paraboloid resembling the curvature of the radome plus a flat continuation into a square at the corners. The shape of the paraboloid has been obtained by measuring the elevation of the bulging radome at several points and performing a least-squares fit. In Fig. 2, the z-axis is magnified in order to highlight the paraboloidal variation of $\tilde{S}$ across the aperture. The curvature of the radome is roughly recognizable also in Fig. 1.

B. Source Reconstruction from Planar NF Measurements

In this work, the SEP is numerically evaluated for electric and magnetic dipole sources of infinitesimal extent on $\tilde{S}$. The positions of the according $\boldsymbol{J}_{\tilde{S}}$ and $\boldsymbol{M}_{\tilde{S}}$ are determined by projecting a square uniform grid with N^2 points onto $\tilde{S}$, where N is chosen as $N = 401$. Correspondingly, the distance between two neighboring current elements is less than $\lambda_0/7$ on the uniform grid. Due to the only slight radome curvature, the spatial density of the current elements with respect to λ_0 does not change significantly. Denoting the complex excitation coefficients of the tangential electric and magnetic surface current elements which reside only on $\tilde{S}$ by $J_{\tilde{S},i}$ and $M_{\tilde{S},i}$, we obtain

$$\boldsymbol{J}_{\tilde{S}}(\boldsymbol{r}') = \sum_{i=1}^{2N^2} J_{\tilde{S},i}\,\boldsymbol{d}_i\,\delta(\boldsymbol{r}'-\boldsymbol{r}_i) \tag{2}$$

and

$$\boldsymbol{M}_{\tilde{S}}(\boldsymbol{r}') = \sum_{i=1}^{2N^2} M_{\tilde{S},i}\,\boldsymbol{d}_i\,\delta(\boldsymbol{r}'-\boldsymbol{r}_i), \tag{3}$$

where $\boldsymbol{r}_i$ are the respective positions of the current elements on $\tilde{S}$. The factor of 2 in the upper sum limits corresponds to the consideration of two orthogonal electric and magnetic current components at every $\boldsymbol{r}_i$. Formally, the orientation $\boldsymbol{d}_i$ of the i-th electric or magnetic current element fulfills

$$\boldsymbol{n}_{\tilde{S}}(\boldsymbol{r}')\cdot\boldsymbol{d}_i = 0 \quad \forall i \in 1,\dots,2N^2 \tag{4a}$$

$$\wedge \quad \boldsymbol{d}_i\cdot\boldsymbol{d}_{i+N^2} = 0 \quad \forall i \in 1,\dots,N^2, \tag{4b}$$

where the normal vector on $\tilde{S}$ is denoted by $\boldsymbol{n}_{\tilde{S}}(\boldsymbol{r}')$. By (4a), it is ensured that all current elements are oriented tangentially to the bulged $\tilde{S}$, see Fig. 2, which is close to, but not exactly a plane. The first N^2 orientations are chosen such that they are parallel to the dominant polarization of the incident field from the antenna. The orthogonality of the electric and magnetic co- and cross-polarized components at every $\boldsymbol{r}'$ is then expressed by (4b). Note that with this definition, there are four current elements at every $\boldsymbol{r}_i$ on the bulged $\tilde{S}$ with respective orientations $\boldsymbol{d}_i$. The corresponding coefficients $J_{\tilde{S},i}$ and $M_{\tilde{S},i}$ are left to be determined.

Incorporating a standard planar NF measurement procedure, the NF is sampled at K regular known positions in front of the aperture in a planar square area slightly extending beyond the radome borders sideways. In the horizontal direction, the NF scanning plane measures slightly below 40 cm. Since the positioner of the used NF scanning environment only allows for a maximum vertical scanning range of only 30 cm, a vertical strip of missing data over a few centimeters is introduced. However, this is not considered to cause significant errors to the electromagnetic drop model to be proposed later.

For every setup under investigation, i.e., with the AUT under dry or wet conditions, two individual measurement runs are performed with the probe rotated by 0° and 90°, respectively, in order to capture both radiated polarization components. In all measurements, the horizontal polarization of the antenna is fed while the other port is terminated with a broad-band $50\,\Omega$ load. As expected, the measured co-polarized NF component is significantly larger in magnitude than the cross-polarized counterpart overall. However, the latter is still reasonably detected. After completing the measurements for both polarizations, the current coefficients are determined by efficiently solving the associated optimization problem

$$\min_{\boldsymbol{J},\boldsymbol{M}\,\in\,\mathbb{C}^{2N^2\times 1}} \left\| \begin{bmatrix}\boldsymbol{A}_\mathrm{e} & Z_\mathrm{F}\boldsymbol{A}_\mathrm{m}\end{bmatrix}\begin{bmatrix}\boldsymbol{J}\\ \boldsymbol{M}\end{bmatrix} - \boldsymbol{b}\right\|_2, \tag{5}$$

where $\boldsymbol{A}_\mathrm{e} \in \mathbb{C}^{K\times 2N^2}$ and $\boldsymbol{A}_\mathrm{m} \in \mathbb{C}^{K\times 2N^2}$ are operators mapping the electric and magnetic current coefficients $J_{\tilde{S},i}$ and $M_{\tilde{S},i}$, collected in $\boldsymbol{J} \in \mathbb{C}^{2N^2\times 1}$ and $\boldsymbol{M} \in \mathbb{C}^{2N^2\times 1}$, to the NF observations $\boldsymbol{b} \in \mathbb{C}^{K\times 1}$ through the corresponding Green's functions [27]. The free-space impedance is denoted as Z_F. For the sake of brevity, (5) is condensed into

$$\min_{\boldsymbol{z}\,\in\,\mathbb{C}^{4N^2\times 1}} \left\|\boldsymbol{A}\boldsymbol{z}-\boldsymbol{b}\right\|_2 \tag{6}$$

with the composite NF operator $\boldsymbol{A}$ and the vector of unknowns $\boldsymbol{z} = \begin{bmatrix}\boldsymbol{J}^\mathrm{T} & \boldsymbol{M}^\mathrm{T}\end{bmatrix}^\mathrm{T}$.

C. NF Measurements of Dry and Wet AUT

While the dry AUT measurement is straightforward, wetness on the radome was imitated by attaching a sheet of thin plastic

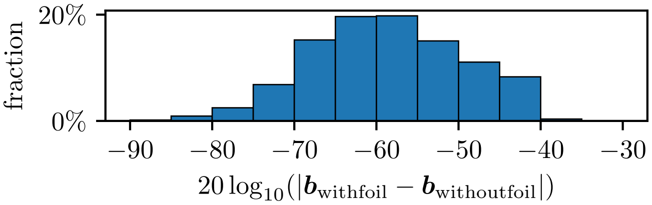

Fig. 3. Histogram of the magnitude of the complex difference of the NF measurement results of the dry AUT alone and the dry AUT with dry bubble foil attached. Occurrences of values below $-90\,\text{dB}$ are excluded from the visualization.

bubble foil to the radome where individual bubbles have been pseudo-randomly injected with distilled water, see Fig. 1. This procedure was chosen so that the drop pattern does not change due to drying or run-off during the NF measurement duration. The approximate diameter of the bubbles is 5 mm, corresponding to already large but still realistic drops. The dielectric properties of distilled water are considered to be equivalent to those of rainwater. Prior to the start of a wet measurement, the bubble foil with the drops was left in the measurement setup for several hours in order to avoid measurements during the first and more dynamic phase of the generally slow-enough evaporation process over time. Furthermore, since the dielectric behavior of water is in general not only a function of frequency but also depends on temperature [28], this time period also allows the water drops to settle to the temperature of the environment, specifically 22°C, to ensure consistent measurement results.

To verify that the bubble foil itself does not introduce significant deviations from the dry NF measurement results, an additional measurement was performed with dry bubble foil attached to the radome, that is, without any water injected. The magnitude of the complex difference between the corresponding measurement result and that of the AUT with the dry radome without any bubble foil is demonstrated in Fig. 3. With the difference generally below $-35\,\text{dB}$ and below $-40\,\text{dB}$ for 99.6% of all NF samples, the impact of the plastic bubble foil alone is found to be negligible.

The solution vectors always contain elements with nonzero magnitude even outside the area of the radome. Due to their low magnitude and similar appearance in all obtained $\boldsymbol{z}$, they are considered to be artifacts created by the solver and, therefore, set to zero.

All panels in Fig. 4 visualize magnitudes of electric or magnetic ESCs on $\tilde{S}$ after projection onto the supporting square plane. Brighter colors correspond to larger ESC magnitudes. The index ”cp” or ”xp” indicates co- or cross-orientation of the respective current elements with respect to the predominantly horizontal polarization of the incident field from the antenna. The apparent truncation in the upper part is due to the limited positioner reach as was described in Section II-B. Outer circular solid lines indicate the actual radome boundary. Along the dashed lines, the parabolic main reflector transitions to a flat metallic ring parallel to the drawing plane behind the radome, which allows the radome to be physically attached to the AUT. Inside the projected area of the metallic ring, i.e., between the solid and dashed circles, the tangential ESCs are practically zero. Therefore, significant ESC magnitudes almost exclusively exist within the indicated dashed circular boundaries.

Figures 4(a)-(d) show the ESC magnitudes for the dry case. The ESC magnitudes obtained from the measurement under wet conditions as depicted in Fig. 1 are shown in Figs. 4(e)-(h). Direct comparison with Fig. 1(b) reveals a strong correspondence between the locations of the water drops on the radome and the spatial distribution of circular patterns in the dominant electric and magnetic ESC components. This observable significant local attenuation in areas which are occupied by drops is attributed to a composition of local absorption and scattering of the energy from the incident electromagnetic field. Note that the intensity of absorption transitions from the inner to the outer border of every drop and extends even beyond the actual drop boundary. Therefore, closely spaced drops appear slightly blurred into each other.

III. DROP MODEL FROM WET NF MEASUREMENTS

A. Procedure

Based on the observations in Section II-C, a simple electromagnetic drop model is proposed and evaluated. With the support of image processing methods, the drop positions held in place by the plastic foil are extracted from a front-view photo of the measurement setup, see, e.g., Fig. 1(b), which had been taken immediately before starting the NF measurement. The extracted drop distribution is stored in the vector $\boldsymbol{w} \in \mathbb{B}^{N^2\times 1}$ according to

$$w_i = \begin{cases} 0, & \text{if } \boldsymbol{r}_i \text{ inside the circular area of a drop,} \\ 1, & \text{else,} \end{cases} \tag{7}$$

taking the known bubble diameter of the foil into account together with the gradually decreasing attenuation towards the outer border of the drops. Then, the previously obtained dry solution $\boldsymbol{z}_{\text{dry}}$ is modified into $\boldsymbol{W}\boldsymbol{z}_{\text{dry}}$ with

$$\boldsymbol{W} = \operatorname{diag}(\boldsymbol{w})_4, \tag{8}$$

where the notation with four copies of $\boldsymbol{w}$ on the main diagonal of $\boldsymbol{W}$ emphasizes that at every $\boldsymbol{r}_i$, which is associated to the inner of a water drop, all four current components, that is, both components of electric and magnetic currents, are set to zero. The resulting $\boldsymbol{W}\boldsymbol{z}_{\text{dry}}$ is shown in Figs. 4(i)-(l) for direct comparison with Figs. 4(e)-(h) or also the photos in Fig. 1.

Obviously, the model identifies the interaction of every single drop with the incident field with the total absorption of energy in the complete circular area which the drop occupies on $\tilde{S}$. All other effects such as the interaction of individual drops with other drops as well as with the antenna itself are not accounted for. Thus, the developed model shares similarities with PO where coupling and edge effects are ignored. Consequently, the approximations made here allow to treat the impact of individual drops linearly and, as will be pointed out, lead to an overall linear and reasonably accurate paradigm for estimating the WAA which is induced by an exemplary drop distribution on the antenna radome.

This article has been accepted for publication in IEEE Transactions on Antennas and Propagation. This is the author's version which has not been fully edited and content may change prior to final publication. Citation information: DOI 10.1109/TAP.2025.3573879

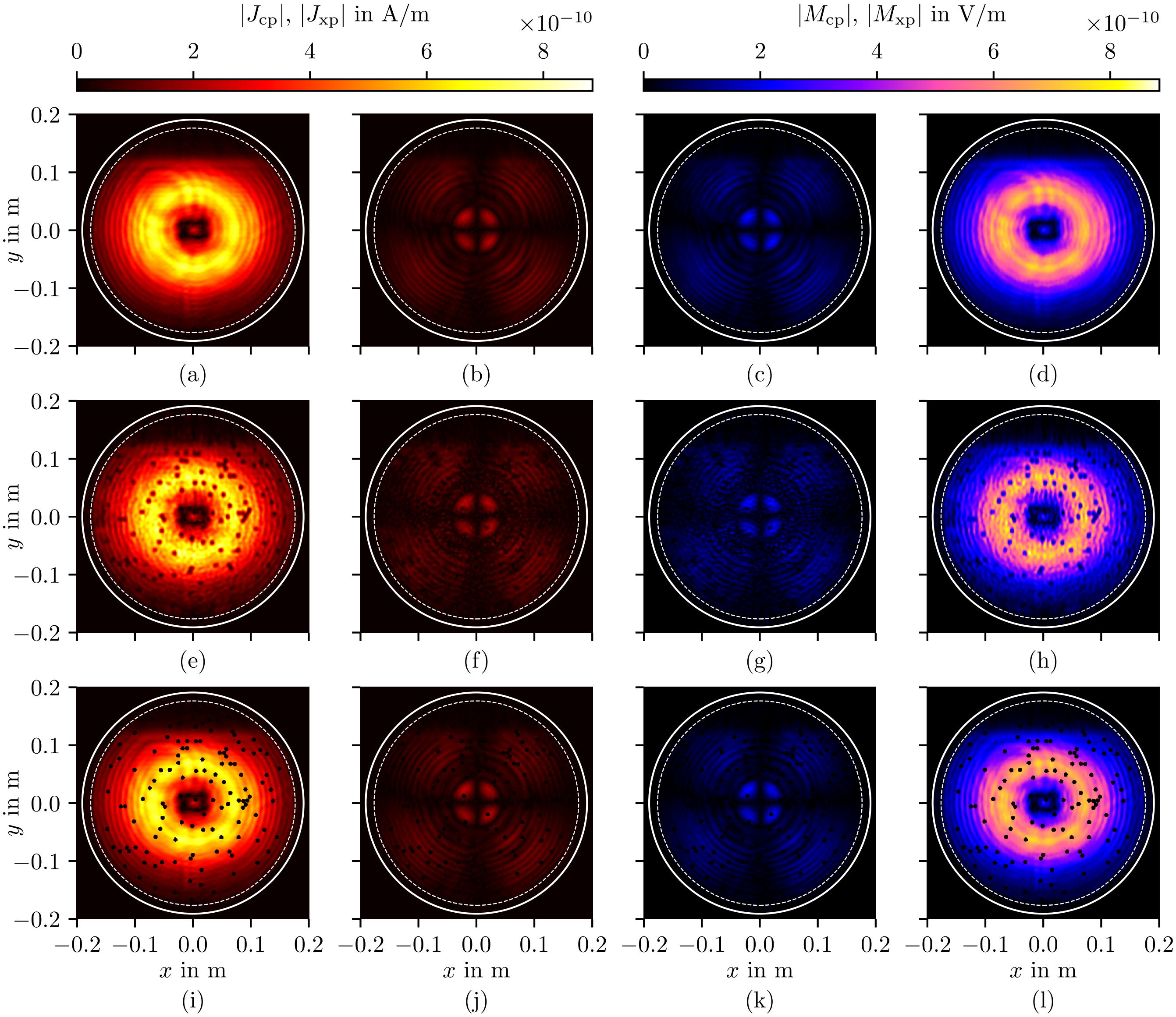

Fig. 4. Magnitude of the equivalent electric and magnetic current elements, (a)-(d) measurement of the dry antenna, (e)-(h) measurement of the wet antenna, (i)-(l) measurement of the dry antenna where individual current coefficients are set to zero in line with the described drop model. The first two columns represent the coefficients of the two orthogonal components of the electric currents, while the last two columns represent the magnetic current coefficients.

B. FF Evaluation

Given the current element coefficients $\boldsymbol{z}$, the radiation operator F is introduced which evaluates the magnitude of the Poynting vector $S(\boldsymbol{k})$ at a large distance from the result of (1) as

$$S(\boldsymbol{k}) = F(\boldsymbol{z}) = \frac{|\boldsymbol{E}_\vartheta(\vartheta,\varphi)|^2 + |\boldsymbol{E}_\varphi(\vartheta,\varphi)|^2}{2\,Z_{\mathrm{F}}}, \tag{9}$$

where the vector $\boldsymbol{k}$ is the direction of interest, determined by the angles ϑ and φ, and $\boldsymbol{E}_\vartheta$, $\boldsymbol{E}_\varphi$ denote the electric field vectors. Figure 5(a) shows the magnitude of the total electric field $E_{\mathrm{t}}(\vartheta_0,\varphi) = \sqrt{2\,Z_{\mathrm{F}}S(\boldsymbol{k})}$ in the cut $\vartheta = \vartheta_0$ through the main lobe $(\vartheta_0,\varphi_0) = (90.21°, 89.71°)$. A zoomed version demonstrating the very narrow main lobe is provided in Fig. 5(b). Due to the necessarily finite NF scanning area, E_{t} is only meaningful inside the angular region around $(\vartheta_0 \pm \alpha_{\mathrm{v}}, \varphi_0 \pm \alpha_{\mathrm{v}})$, where α_{v} can, according to [29], [30], be estimated by

$$\alpha_{\mathrm{v}} = \arctan\left(\frac{L-2R}{2D}\right), \tag{10}$$

with L, R, and D corresponding to the side length of the scan area, the radius of the aperture, and the distance from the NF measurement plane to the aperture, respectively. Due to the incomplete NF scan over the vertical dimension of the aperture as mentioned earlier, the estimated α_{v} would, however, become negative if the shorter side length would be used for L. Therefore, L is set to the horizontal extent of the measurement plane, which is slightly under 40 cm, see Section II-B. Together with the largest distance to the bulged aperture, (10) then yields a value of $\alpha_{\mathrm{v}} \approx 11.7°$. This estimated valid region, highlighted in light blue in Fig. 5(a), encloses the FF region of strong radiation sufficiently well.

This article has been accepted for publication in IEEE Transactions on Antennas and Propagation. This is the author's version which has not been fully edited and content may change prior to final publication. Citation information: DOI 10.1109/TAP.2025.3573879

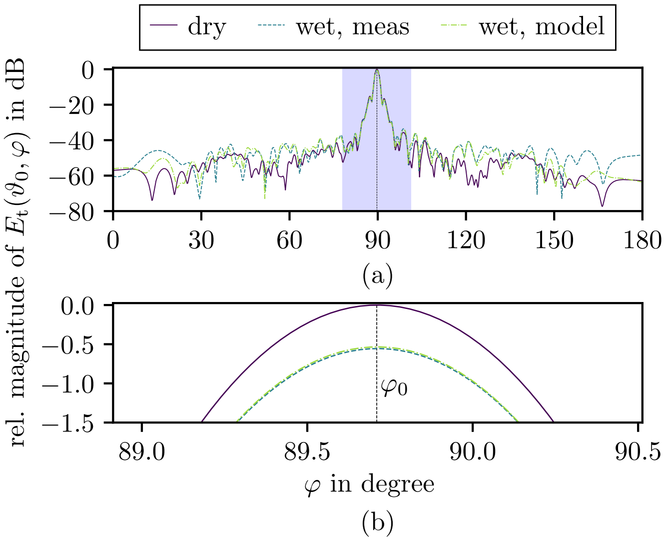

Fig. 5. Magnitude of the electric field $E_\mathrm{t}(\vartheta, \varphi)$ for $\vartheta = \vartheta_0$ at a large distance of the dry antenna, normalized to the magnitude maximum of the dry electric field in main lobe direction. (a) Cut with the valid angular region highlighted in light blue, (b) zoomed version (without highlighting). The slight angular offset of the main lobe, i.e., $\varphi_0 \neq 90°$, is attributed to an imperfect alignment of the AUT in the measurement setup.

Furthermore, since negligibly small NF intensities have been observed close to almost the full border of the scan plane, the truncation of the measurement plane is not considered to induce significant errors overall.

C. Evaluation of the Model in Boresight Direction

Only looking into the boresight direction $\boldsymbol{k}_0$ of the AUT determined by the angles ϑ_0 and φ_0, the operator F_0 is defined as a special case of (9). In order to assess WAA, the Poynting vector magnitude $S(\boldsymbol{k_0}) = F_0(\boldsymbol{z})$ is used, where it is, correspondingly, assumed that the hypothetically involved second CML antenna is perfectly aligned to the first one, which is under investigation. The WAA value $A_\mathrm{W,meas}$, which is caused by the water drops, is denoted in dB as

$$A_\mathrm{W,meas} = 10\log_{10}(F_0(\boldsymbol{z}_\mathrm{wet})) - B, \tag{11}$$

and the value $A_\mathrm{W,model}$, obtained from the drop model, is

$$A_\mathrm{W,model} = 10\log_{10}(F_0(\boldsymbol{W}\boldsymbol{z}_\mathrm{dry})) - B, \tag{12}$$

both with the dry reference value

$$B = 10\log_{10}(F_0(\boldsymbol{z}_\mathrm{dry})). \tag{13}$$

The current elements are illuminated approximately equally in phase. Recalling (7), it is, therefore, very intuitive that the modeled WAA increases with the number of zero entries in $\boldsymbol{w}$, corresponding to the number of current elements that are set to zero, or, ultimately, the number of drops on the radome. In the hypothetical case $\boldsymbol{w} = \boldsymbol{0}$, all currents are set to zero. In the sense of this model, this limit could theoretically be interpreted as a continuous water film that absorbs all energy that would be radiated from the dry antenna otherwise. This interpretation, however, depends on the chosen ESC granularity and the occurring drop size distribution, basically constituting a quantization issue. Due to the often chosen hydrophobic radome materials, which usually prevent the formation of continuous water films, this case is rather less relevant, but nevertheless, its implication is worth noting. Similarly, if all elements of $\boldsymbol{w}$ are unity, there would be no radome wetness at all, and it is easy to see that the drop model would reasonably indicate zero dB of WAA.

TABLE I
WAA VALUES FROM THE MEASUREMENT AND FROM THE DROP MODEL.

	few drops	many drops
Measured WAA	0.34 dB	0.56 dB
Modeled WAA	0.32 dB	0.53 dB

Evaluating (11) for the drop distribution as depicted in Figs. 4(e)-(h) yields $A_\mathrm{W,meas} \approx 0.56\,\mathrm{dB}$ while the drop model estimation provides a very close value of $A_\mathrm{W,model} \approx 0.53\,\mathrm{dB}$. A similar experiment with a smaller number of filled bubbles has been carried out where some features of the drop distribution have been retained deliberately, see Fig. 6. For the sake of clarity, the visualizations of the cross-polarized electric and the cross-polarized magnetic current components have been omitted here. The second experiment yields $A_\mathrm{W,meas} \approx 0.34\,\mathrm{dB}$. Replication in the drop model produces $A_\mathrm{W,model} \approx 0.32\,\mathrm{dB}$, likewise matching the measured WAA result closely. Since the setups for the NF measurements were identical, that is, the AUT was not moved between the experiments, both differences to the originally dry case are solely attributed to the WAA induced by the drops inside the bubble foil. The measured and modeled WAA results are summarized in Table I.

The method for WAA estimation also applies to the receiving antenna. If the drop distributions are quantitatively similar, the effective WAA in a link consisting of two antennas would have to be doubled accordingly, based on the reciprocity of transmit and receive. Cognizant of the very close match of the measured and the modeled WAA values in both cases, the proposed model turns out to reflect the effective attenuation in the presence of water sufficiently well.

IV. WAA OF SYNTHETIC DROP DISTRIBUTIONS

The manual wetting of bubble foil is laborious and, therefore, not reasonable to repeat over and over again for the analysis of further individual drop distributions. Based on the justification of the proposed model from the results presented in Section III-C, which are summarized in Tab. I, synthetic drop distributions (SDDs) are investigated as a next step.

During natural dew or precipitation events, drops of various diameters will accumulate at stochastic locations on the radome. As can be seen in, e.g., Figs. 4(a)-(d), the magnitude of the current elements varies notably across the radome area, especially along the radial distance from the (projected) center of the radome. Since the magnitudes are set to zero according to the drop model, there will be a stronger impact on the radiation performance of the AUT if more individual drops

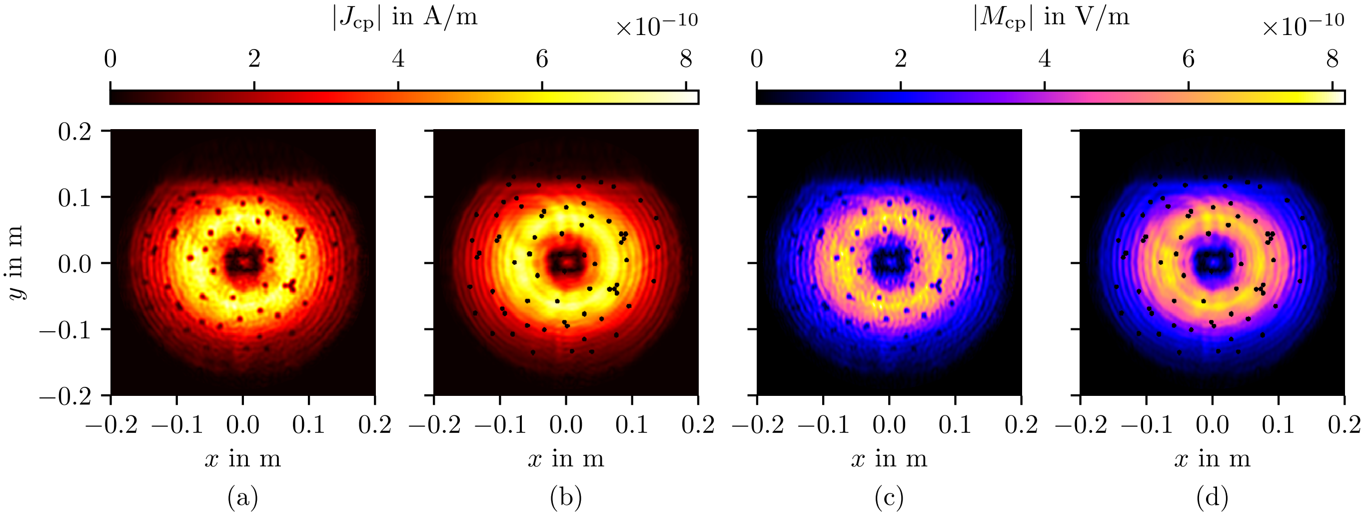

Fig. 6. Magnitude of the equivalent electric current elements, (a) measurement of the wet antenna, (b) replication in line with the drop model, and magnitude of the equivalent magnetic currents, (c) measurement of the wet antenna, (d) replication in line with the drop model. The cross-polarized electric currents and the co-polarized magnetic currents have been omitted from the visualization due to their small magnitude and redundancy, see Fig. 4.

are sitting in those areas with larger ESC magnitude. In order to account for this in a WAA model, detailed information would be needed about the exact drop positions and also on the ESC magnitude across the radome. However, exact knowledge of the drop formation processes at real CML antennas is commonly not available. We assume that, during moistening of a CML antenna due to environmental conditions, the constituting wetness distributes randomly across the complete aperture, yielding a quasi-uniform drop distribution. Particularly, drops do not concentrate in specific areas, e.g., not systematically in those regions where primarily the largest or lowest current element magnitudes are obtained. Visual inspection of numerous camera photos of wet antennas during natural dew and rain as shown in [31] justifies this assumption.

Drop distributions are generated by starting with a plane uniform grid across the aperture area and adding two-dimensional positional noise to every grid node. For SDDs, as they are qualitatively assumed to establish during rain, the drop diameters are chosen randomly between 3 mm and 6 mm for every individual drop. The lower limit of 3 mm was chosen in order to ensure the formation of reasonably large drops during fictitious rain. Moreover, synthetic dew is generated with all droplet diameters chosen as small as possible, corresponding to the region represented by exactly one ESC. For the chosen $N = 401$, all dew droplets share the same diameter of about 1 mm.

After generating random drop information with the described procedure for both considered wetness classes, i.e., each for dew and rain, the generated drops on a plane are projected onto the aperture $\tilde{S}$. Overall, this procedure corresponds to the construction of one $\boldsymbol{w}$-vector as introduced in (7) per random arrangement and modifying $\boldsymbol{z}_{\mathrm{dry}}$ into $\boldsymbol{W}\boldsymbol{z}_{\mathrm{dry}}$ accordingly, while, in contrast, Section III-A described the strategy to replicate an existing drop distribution into a $\boldsymbol{w}$-vector. Evaluation of $F_0(\boldsymbol{W}\boldsymbol{z}_{\mathrm{dry}})$ and using (12) then yields one corresponding WAA value A_{SDD} for each individual SDD.

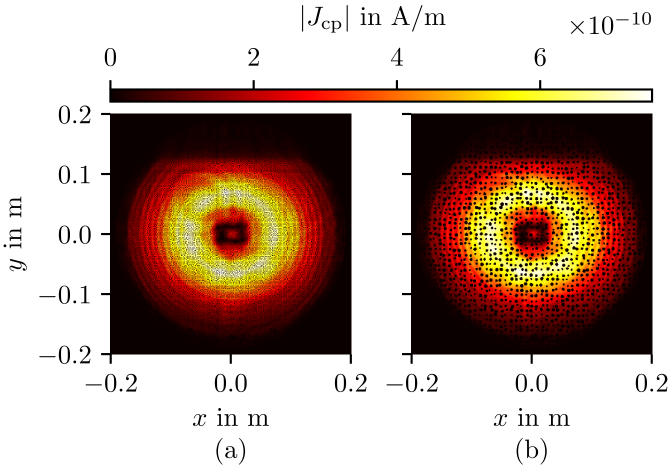

Fig. 7. Examples of SDDs after application of randomly determined drop positions and diameters in the sense of the drop model. (a) Intense dew with the smallest possible drop diameter of 1 mm for the choice $N = 401$, (b) raindrops in the case of heavy rainfall with random diameters between 3 mm and 6 mm.

The relative aperture area which is occupied by all drops together is reflected in the total amount of current elements set to zero due to synthetic water drops divided by the total number of current elements across the aperture. This ratio will be referred to as a in the following.

For $P = 20$ individual severities of wetness, i.e., numbers of synthetic drops, $Q = 25$ realizations were generated for dew and rain each to investigate changes due to variations of the drop positions and, in the case of rain, also of the drop diameters. Figures 7(a) and (b) illustrate one example SDD for very intense dew and rain, respectively, by means of the accordingly modified dry ESC distribution. Although these examples clearly appear differently since they represent different classes of radome wetness, both correspond to the same relative radome area $a \approx 22\%$ which is covered by

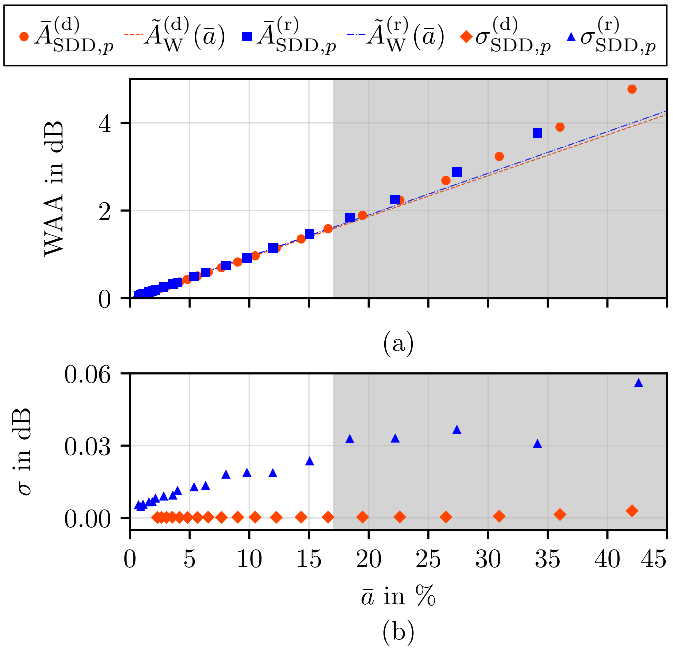

(a)

(b)

Fig. 8. Single-antenna WAA results for the SDDs. (a) WAA median data points with linear fits in dB. (b) Corresponding standard deviations.

drops, i.e., more than one fifth of the currents are set to zero. Particularly in the dew example, the quantization of the current element positions becomes visible. For larger N, even finer dew SDDs would, however, be possible theoretically. The rain example already shows several overlapping drop pairs, which would naturally combine into one larger drop and potentially run off. These observations make this value for a, together with $N = 401$, a limit case which would most probably not constitute naturally, especially in the case of rain.

Due to the random generation of drops, all SDDs for the p-th wetness level come up with slightly different values a_{pq}, $q = 1, \dots, Q$. Therefore, the medians $\bar{a}_p$ are determined as

$$\bar{a}_p = \mathrm{med}\left\{a_{pq}\right\}_{q=1}^{Q}, \quad p = 1, \dots, P. \tag{14}$$

Altogether, $PQ = 500$ random examples are investigated for dew and rain individually. The Q correspondingly observed WAA values $A^{(\mathrm{d/r})}_{\mathrm{SDD},a_{pq}}$ for one specific p, where the superscripts "(d)" and "(r)" indicate dew or rain, respectively, are summarized using the median into

$$\bar{A}^{(\mathrm{d/r})}_{\mathrm{SDD},p} = \mathrm{med}\left\{A^{(\mathrm{d/r})}_{\mathrm{SDD},a_{pq}}\right\}_{q=1}^{Q}, \quad p = 1, \dots, P. \tag{15}$$

The resulting data points $\left(\bar{a}_p, \bar{A}^{(\mathrm{d/r})}_{\mathrm{SDD},p}\right)$ are shown in Fig. 8(a) for all considered drop amounts. Below the data point at $\bar{a} \approx 22\%$, approximately quadratic relationships of the WAA medians for dew and rain are observed, respectively, which are fitted to linear functions $\tilde{A}^{(\mathrm{d/r})}_{\mathrm{W}}(\bar{a})$ in dB in the visualization. In order to ensure zero WAA for $a = \bar{a} = 0$, this data point is added to the regression with an increased weighting factor. The slopes for dew and rain are virtually equal, suggesting that WAA from the drops can be modeled even without knowledge of the considered wetness class. Therefore, WAA can universally be estimated for dew and rain by

$$\tilde{A}_{\mathrm{W}}(a) = \Psi a \tag{16}$$

in dB, where $\Psi \approx 0.094\,\mathrm{dB}/\%$ is the slope of the linear estimation function for both wetness classes.

Restricting ourselves to realistic drop amounts, i.e., to those data points with $\bar{a} \leq 17\%$ in order to introduce an exemplary margin of 5% to the abovementioned 22%, we reach about $1.6\,\mathrm{dB}$ of WAA for a still severely moistened antenna radome. By inspection of wet radome pictures from the dataset generated by the field experiment [31], [32], this value appears appropriate for large rainfall intensities. The range of $\bar{a}$ is grayed out correspondingly for $\bar{a} > 17\%$.

On the basis of reciprocity, (16) must be evaluated for both antennas involved in a CML as mentioned in Section III-C. Doubling the WAA result accordingly yields WAA estimations of effectively up to $3.2\,\mathrm{dB}$ WAA for an actual CML, which is a reasonable value according to previous studies [16], [18]. Therefore, for reasonable drop amounts sufficiently below that of the limit cases, the presented water drop model will always lead to plausible WAA values. For increasing values of $\bar{a}$, the WAA increases more and more disproportionately over $\bar{a}$, see the area shaded in gray in Fig. 8(a), approaching the aforementioned limit of infinite WAA for $\bar{a} \to 1$. This extreme case is not included in the visualization.

Note that the standard deviations

$$\sigma^{(\mathrm{d/r})}_{\mathrm{SDD},p} = \mathrm{std}\left\{A^{(\mathrm{d/r})}_{\mathrm{SDD},a_{pq}}\right\}_{q=1}^{Q}, \quad p = 1, \dots, P, \tag{17}$$

are neglectable for all considered examples, especially for dew, see Fig. 8(b). This altogether indicates that the actual drop positions are less relevant for WAA than the total drop amount. However, this observation strongly relies on the fact that the drops are quasi-uniformly distributed over the aperture area, which is usually the case as was pointed out earlier. Then, on average, the same amount of current elements with weak and large magnitudes (in the dry case) are attenuated by the drops, respectively. Particularly this leads to the convenient linear WAA estimation in dB over the relative radome area which is occupied by water drops.

In order to apply the model for actual WAA correction in a real CML, this information still would have to be obtained from other sources of data, e.g., the antenna reflection coefficient, which has been shown to be sensible to the amount of radome wetness [14], [31]–[33].

V. CONCLUSION

A simple and intuitive electromagnetic model for individual water drops on a large antenna radome has been deduced from NF measurements of an AUT under dry and wet conditions. In order to approximately replicate the observed effects on the measurements which are induced by water drops, the determined equivalent radiating current elements of the dry AUT were set to zero everywhere inside areas of physically present drops which were attached in a separate experiment. The corresponding radiated power density in boresight direction reproduced the result from the associated measurement with sufficient accuracy in two individual passes. The difference relative to the dry result is precisely the WAA. Subsequent investigation of synthetic but realistic drop distributions, based on visual inspection of numerous photos of wet antennas during natural dew and rain, revealed linear relationships of the WAA (in decibels) with the relative portion of the radome area occupied by drops. The slopes for dew and rain were almost identical. Among several individual drop distribution examples, the WAA variability was negligible for the same individually considered wetness level, especially in the case of dew. This observation suggests that the specific drop locations are not relevant if the drops are distributed quasi-uniformly across the radome. Therefore, the resulting linear model is based on the assumption of a nearly uniform drop distribution on the radome area. However, for realistic CMLs, this is usually guaranteed since the formation process of drops is of stochastic nature and, thus, the drops will not systematically concentrate on particular areas of the aperture.

Despite the potential of the proposed method for the development of future WAA correction models, there are also limitations. Since information on the aperture area which is covered by water drops is commonly not (directly) available in real CMLs, the proposed paradigm cannot directly be used to correct for the WAA in CML time series. An adequate assessment of the water amount on the radome would be required, which is usually difficult and would need further careful evaluation. Furthermore, the presented linear model is tailored to the antenna at hand and not yet agnostic regarding parameters such as the operating frequency.

However, this work has established a basis for new WAA estimation models and techniques, characterized by a conceptual relationship to electromagnetics. In future work, further experiments will be performed using more frequencies and antennas. Detailed inspection of potentially frequency-dependent interaction characteristics of water residuals with the incident electromagnetic field from the antenna will allow to generalize and advance the drop modelling technique. This continued development of the model will further improve the understanding of the physical processes that constitute WAA and should ultimately culminate in new methods for WAA estimation and correction for rainfall estimation in CML time series.

VI. ACKNOWLEDGMENT

The authors thank Dr. Bernd Hofmann for helping with the NF measurements.

REFERENCES

[1] H. Messer, A. Zinevich, and P. Alpert, "Environmental Monitoring by Wireless Communication Networks," *Science*, vol. 312, no. 5774, May 2006.

[2] H. Leijnse, R. Uijlenhoet, and J. N. M. Stricker, "Rainfall measurement using radio links from cellular communication networks," *Water Resources Research*, vol. 43, no. 3, Mar. 2007.

[3] M. Graf, C. Chwala, J. Polz, and H. Kunstmann, "Rainfall estimation from a German-wide commercial microwave link network: Optimized processing and validation for 1 year of data," *Hydrology and Earth System Sciences*, vol. 24, no. 6, Jun. 2020.

[4] A. Overeem, H. Leijnse, T. C. van Leth, L. Bogerd, J. Priebe, D. Tricarico, A. Droste, and R. Uijlenhoet, "Tropical rainfall monitoring with commercial microwave links in Sri Lanka," *Environmental Research Letters*, vol. 16, no. 7, Jul. 2021.

[5] M. Djibo, C. Chwala, M. Graf, J. Polz, H. Kunstmann, and F. Zougmoré, "High-resolution rainfall maps from commercial microwave links for a data-scarce region in West Africa," *Journal of Hydrometeorology*, vol. 24, no. 10, 2023.

[6] M. Fencl, J. Rieckermann, M. Schleiss, D. Stránský, and V. Bareš, "Assessing the potential of using telecommunication microwave links in urban drainage modelling," *Water Science and Technology*, vol. 68, no. 8, 10 2013.

[7] M. Turko, M. Gosset, M. Kacou, C. Bouvier, N. Chahinian, A. Boone, and M. Alcoba, "Rainfall measurement from commercial microwave links for urban hydrology in Africa: A simulation framework for sensitivity analysis," *Journal of Hydrometeorology*, vol. 22, no. 7, 2021.

[8] O. Harel, N. David, P. Alpert, and H. Messer, "The potential of microwave communication networks to detect dew—experimental study," *IEEE Journal of Selected Topics in Applied Earth Observations and Remote Sensing*, vol. 8, no. 9, 2015.

[9] N. David, O. Harel, P. Alpert, and H. Messer, "Study of attenuation due to wet antenna in microwave radio communication," in *IEEE International Conference on Acoustics, Speech, and Signal Processing*, Shanghai, Mar. 2016.

[10] B. Blevis, "Losses due to rain on radomes and antenna reflecting surfaces," *IEEE Transactions on Antennas and Propagation*, vol. 13, no. 1, 1965.

[11] H. Leijnse, R. Uijlenhoet, and J. Stricker, "Microwave link rainfall estimation: Effects of link length and frequency, temporal sampling, power resolution, and wet antenna attenuation," *Advances in Water Resources*, vol. 31, no. 11, Nov. 2008.

[12] A. Mancini, R. M. Lebrón, and J. L. Salazar, "The impact of a wet S-band radome on dual-polarized phased-array radar system performance," *IEEE Transactions on Antennas and Propagation*, vol. 67, no. 1, 2019.

[13] J. Tiede, U. Siart, and T. F. Eibert, "Doubly-periodic unit cell modeling of the frequency-dependent transmission and reflection behavior of large aperture antenna radomes wetted by water drops," in *IEEE International Symposium on Antennas and Propagation and INC/USNC-URSI Radio Science Meeting (AP-S/INC-USNC-URSI)*, Florence, Italy, Jul. 2024.

[14] C. Moroder, U. Siart, C. Chwala, and H. Kunstmann, "Modeling of wet antenna attenuation for precipitation estimation from microwave links," *IEEE Geoscience and Remote Sensing Letters*, vol. 17, no. 3, Mar. 2020.

[15] A. Overeem, H. Leijnse, and R. Uijlenhoet, "Two and a half years of country-wide rainfall maps using radio links from commercial cellular telecommunication networks," *Water Resources Research*, vol. 52, no. 10, 2016.

[16] M. Schleiss, J. Rieckermann, and A. Berne, "Quantification and modeling of wet-antenna attenuation for commercial microwave links," *IEEE Geoscience and Remote Sensing Letters*, vol. 10, no. 5, Sep. 2013.

[17] J. Pastorek, M. Fencl, J. Rieckermann, and V. Bareš, "Precipitation estimates from commercial microwave links: Practical approaches to wet-antenna correction," *IEEE Transactions on Geoscience and Remote Sensing*, vol. 60, 2022.

[18] P. Valtr, M. Fencl, and V. Bareš, "Excess attenuation caused by antenna wetting of terrestrial microwave links at 32 GHz," *IEEE Antennas and Wireless Propagation Letters*, vol. 18, no. 8, 2019.

[19] M. Fencl, P. Valtr, M. Kvičera, and V. Bareš, "Quantifying wet antenna attenuation in 38-GHz commercial microwave links of cellular backhaul," *IEEE Geoscience and Remote Sensing Letters*, vol. 16, no. 4, Apr. 2019.

[20] K. Pu, X. Liu, and H. He, "Wet antenna attenuation model of E-band microwave links based on the LSTM8 algorithm," *IEEE Antennas and Wireless Propagation Letters*, vol. 19, no. 9, 2020.

[21] N. Blettner, M. Fencl, V. Bareš, H. Kunstmann, and C. Chwala, "Transboundary rainfall estimation using commercial microwave links," *Earth and Space Science*, vol. 10, no. 8, 2023.

[22] F. Sáez de Adana, Ed., *Practical Applications of Asymptotic Techniques in Electromagnetics*, ser. Artech House Electromagnetics series. Boston, MA, USA: Artech House, 2011.

[23] P. Y. Ufimtsev, *Fundamentals of the Physical Theory of Diffraction*, 1st ed. Hoboken, NJ, USA: John Wiley & Sons, May 2014.

[24] C. Koenen, G. Hamberger, U. Siart, and T. F. Eibert, "A volumetric near-field scanner for millimeter-wave antenna measurements," in *10th European Conference on Antennas and Propagation (EuCAP)*, Davos, Switzerland, Apr. 2016.

[25] G. F. Hamberger, C. Koenen, O. Neitz, R. A. M. Mauermayer, C. J. Eisner, U. Siart, and T. F. Eibert, "Setup and characterization of

a volumetric W-band near-field antenna measurement system," *IEEE Transactions on Antennas and Propagation*, vol. 66, no. 10, 2018.

[26] J.-M. Jin, *Theory and Computation of Electromagnetic Fields*, 2nd ed. Hoboken, NJ, USA: John Wiley & Sons, 2015.

[27] A. Paulus and T. F. Eibert, "Brute-force GPU accelerated evaluation of dipole-dipole interactions," in *IEEE International Symposium on Antennas and Propagation & USNC/URSI National Radio Science Meeting*, Boston, MA, USA, Jul. 2018.

[28] P. J. W. Debye, *Polare Molekeln*. Leipzig, Germany: Hirzel, 1929.

[29] A. C. Newell and M. L. Crawford, "Planar near-field measurements on high performance array antennas." National Institute of Standards and Technology, Jul. 1974.

[30] A. D. Yaghjian, "Upper-bound errors in far-field antenna parameters determined from planar near-field measurements. Part 1: Analysis," *NASA STI/Recon Technical Report N*, vol. 76, Oct. 1975.

[31] J. Tiede, C. Chwala, and U. Siart, "New insights into the dynamics of wet antenna attenuation based on in situ estimations provided by the dedicated field experiment ATTRRA2," *IEEE Geoscience and Remote Sensing Letters*, vol. 20, 2023.

[32] C. Moroder, U. Siart, C. Chwala, and H. Kunstmann, "Microwave instrument for simultaneous wet antenna attenuation and precipitation measurement," *IEEE Transactions on Instrumentation and Measurement*, vol. 69, no. 8, Aug. 2020.

[33] J. Tiede, C. Chwala, U. Siart, and T. F. Eibert, "Frequency-dependent variations of the antenna reflection coefficient due to different wetness conditions on the antenna radome," *Advances in Radio Science*, vol. 23, 2025.

Jonas Tiede (Graduate Student Member, IEEE) received the B.Sc. and the M.Sc. in electrical engineering and information technology from the Technical University of Munich, Munich, Germany, in 2017 and 2020. Since 2020, he has been working as a Research Assistant at the Chair of High-Frequency Engineering, Department of Electrical Engineering, School of Computation, Information and Technology, Technical University of Munich. His current research interests include electromagnetic wave propagation under atmospheric conditions, antenna measurement techniques, near-field far-field transformations, and remote sensing.

Christian Chwala received the Diploma degree in physics from the University of Regensburg, Regensburg, Germany, in 2008, and the Dr.rer.nat. degree in climate and environmental science from the University of Augsburg, Augsburg, Germany, in 2015. His work focuses on the usage of opportunistic rainfall sensors and merging of weather radar data with ground-based observations for which he also applies data-driven methods. He currently leads several research projects in this field at Karlsruhe Institute of Technology (KIT), Campus Alpin, Garmisch-Partenkirchen, Germany.

Christian Herpers received his B.Eng. in electrical engineering and information technology from the Munich University of Applied Sciences, Munich, Germany, in 2022 and completed his M.Sc.E. in electrical engineering at the University of New Brunswick, Fredericton, NB, Canada, in 2023. From 2017 to 2022, he was a Dual and Working Student with Rohde & Schwarz, Munich and from 2022 to 2023, a Research and Teaching Assistant with the University of New Brunswick. Since 2024, he has been with the Technical University of Munich and joined the Fraunhofer EMFT Institute for Electronic Microsystems and Solid State Technologies as a Research Assistant in 2025. His research interests include electrostatic discharge, RF measurements, and wireless power.

Alexander H. Paulus (Member, IEEE) received the M.Sc. and Dr.-Ing. degrees in electrical engineering and information technology from the Technical University of Munich, Munich, Germany, in 2015 and 2022, respectively. Since 2022, he has been working as a Senior Researcher at the Chair of High-Frequency Engineering, Department of Electrical Engineering, School of Computation, Information and Technology, Technical University of Munich. From 2024 to 2025, he has been a Visiting Researcher at the Politecnico di Milano, Milan, Italy. His research interests include inverse electromagnetic problems, computational electromagnetics, and antenna measurement techniques.

Uwe Siart received the Dipl.-Ing. degree from the University of Erlangen-Nürnberg, Erlangen, Germany, in 1996 and the Dr.-Ing. degree from the Technical University of Munich, Munich, Germany, in 2005. He has been with the Chair of High-Frequency Engineering within the School of Computation, Information and Technology at the Technical University of Munich since 1996. In 2005, he became a Senior Research Associate. His research interests are in the fields of microwave radar signal processing, high-frequency measurement and testing and passive microwave components. Currently, he is working on electromagnetic sensors for climate-neutral fuel technology and on remote sensing the atmosphere based on microwave point-to-point radio links.

Thomas F. Eibert (Senior Member, IEEE) received the Dipl.-Ing. (FH) degree in electrical engineering from Fachhochschule Nürnberg, Nuremberg, Germany, in 1989, the Dipl.-Ing. degree in electrical engineering from Ruhr-Universität Bochum, Bochum, Germany, in 1992, and the Dr.-Ing. degree in electrical engineering from Bergische Universität Wuppertal, Wuppertal, Germany, in 1997. He is a Full Professor of high-frequency engineering with the Technical University of Munich, Munich, Germany, where he is currently also the Academic Program Director responsible for the study courses in the professional profile electrical and computer engineering.